Investigation of wire-array Z-pinches by laser probing diagnostics

Cite as: Matter Radiat. Extremes 4, 017401 (2019); https://doi.org/10.1063/1.5081453
Submitted: 14 November 2018 • Accepted: 15 November 2018 • Published Online: 17 January 2019

V. V. Ivanov, A. A. Anderson and D. Papp

Matter and Radiation at Extremes

RESEARCH ARTICLE

scitation.org/journal/mre

Investigation of wire-array Z-pinches by laser probing diagnostics

Cite as: Matter Radiat. Extremes 4, 017401 (2019); doi: 10.1063/1.5081453
Submitted: 14 November 2018 • Accepted: 15 November 2018 •
Published Online: 17 January 2019

V. V. Ivanov,[1] A. A. Anderson,[1] and D. Papp[2]

AFFILIATIONS

[1]Department of Physics, University of Nevada, Reno, Nevada 89557, USA
[2]ELI-ALPS, ELI-HU Nkft., H-6720 Szeged, Hungary

ABSTRACT

Laser diagnostics provides powerful tools for the investigation of dense Z-pinches. In this paper, wire-array Z-pinches are investigated at the 1 MA Zebra generator using laser diagnostics at different wavelengths coupled with x-ray diagnostics. Plasma dynamics during the ablation, implosion, and stagnation stages are observed by multiframe diagnostics. Cascading and non-precursor implosions are studied in wire arrays. Ultraviolet diagnostics allows deep penetration into the Z-pinch plasma at stagnation. End-on probing reveals the complicated structure of the precursor. Strong magnetohydrodynamic instabilities are found in a dense pinch hidden in the trailing plasma. Small-scale instabilities are seen in the Z-pinch plasma with micrometer resolution. Probing of the pinch from four directions shows asymmetrical trailing plasma in some configurations of wire arrays. Faraday rotation diagnostics reveals the magnetic fields and the current distribution in the plasma of the precursor and Z-pinch. Redistribution of current in the trailing plasma is seen during kink and sausage instabilities in the stagnation stage. The formation of micropinches and hot spots in the Z-pinch is analyzed with coupled laser and x-ray diagnostics. Different laser diagnostics allow the study of Z-pinch plasmas in all stages, including fast dynamics and instabilities.

I. INTRODUCTION

Z-pinches are efficient laboratory sources of powerful x-ray radiation. They can be applied in a number of areas of high-energy-density laboratory plasma physics, including laboratory astrophysics, atomic and radiation physics and spectroscopy, studies of material properties, and fusion research.[1–5] Although there has been impressive experimental progress in Z-pinch physics and its applications at currents of 10–20 MA, many aspects of the physics of dense Z-pinches can be studied at load currents in the range 1–2 MA.

Laser probing diagnostics has been widely used for investigation of Z-pinch plasmas and to clarify the physical processes involved in Z-pinches. The main stages involved in wire-array Z-pinch and plasma instabilities were elucidated in the first decade of this century.[6–9] The formation of a core–corona structure on wires after flashover and the generation of a periodic plasma jets in the ablation stage was investigated in Ref. 6. Ablation plasma streams reach the center of a cylindrical wire array and form a precursor plasma column. During the implosion stage, the plasma of a cylindrical wire array implodes in a snowplow manner and produces a dense Z-pinch.[7] End-on and side-on probing at a wavelength of 532 nm was applied to study the ablation and implosion stages. The Z-pinch radiates a short powerful x-ray burst during the stagnation stage. The Z-pinch plasma column is highly inhomogeneous owing to the development of strong magnetohydrodynamic (MHD) kink and sausage instabilities. Bright, powerful, and compact x-ray sources termed micropinches or "hot spots" arise in different types of Z-pinch.[10] All of the abovementioned features of wire array Z-pinches have been observed in different machines at load currents from 1 to 10 MA.[11]

The application of multiframe laser diagnostics to Z-pinches has revealed the implosion dynamics in wire arrays. The formation and dynamics of plasma bubbles at the beginning of the implosion stage in cylindrical wire arrays have been studied with side-on probing at 532 nm.[12] Precursor plasma columns in wire arrays have been found to contain fine structures with large- and small-scale instabilities.[13] Cascading of the characteristic size of

instabilities to smaller scales has been linked to flute-mode turbulence in the precursor plasma.[14] Faraday rotation diagnostics has allowed the investigation of magnetic fields and reconstruction of the current distribution in wire arrays. Currents of 0.1–0.2 MA have been measured in the precursor plasma column in the ablation stage.[15] Bubble-like areas with perturbations of the magnetic field have been observed in Faraday images of the precursor plasma. The main features of the formation and evolution of the dense pinch and trailing mass have been studied with laser diagnostics at a wavelength of 532 nm.

Shadowgraphy, interferometry, schlieren, and Faraday rotation diagnostics have provided data about Z-pinch plasmas with electron densities of the order of 10^{19} cm^{-3}. However, laser diagnostics in the optical range cannot be applied to the stagnation phase of Z-pinches owing to strong absorption and refraction of the laser beam in the dense plasma. A laser beam of wavelength 532 nm cannot pass through the trailing plasma and probe the Z-pinch. However, ultraviolet (UV) laser diagnostics has shown promise for the investigation of dense Z-pinch plasmas.[16–18]

In this paper, we describe the investigation of wire-array Z-pinches at the Nevada Terawatt Facility (NTF) at the University of Nevada, Reno (UNR). Laser diagnostics at wavelengths from 213 to 1064 nm have been applied to wire arrays at different phases. Different configurations of wire arrays are studied, including star, linear (planar), and double-cylinder loads. UV high-resolution diagnostics is deployed at the 1 MA Zebra generator and allows detailed investigation of the stagnation stage in a dense Z-pinch. Laser probing includes side-on and end-on shadowgraphy, interferometry, and Faraday rotation diagnostics. Shadowgraphy with a spatial resolution of <5 μm shows microperturbations of the plasma density in the precursor and Z-pinch. Two-frame diagnostics reveals fast plasma motion in the Z-pinch in the stagnation phase. The structure of the magnetic fields is revealed and the redistribution of current in the trailing plasma and Z-pinch is reconstructed using Faraday diagnostics. UV diagnostics reveals the origin of "hot spots" in Z-pinches. Laser probing in four directions reveals strong asymmetry of some wire-array Z-pinches. The dynamics of implosion and stagnation and the development of instabilities in Z-pinches are in agreement with three-dimensional MHD simulations.

II. LASER DIAGNOSTICS FOR Z-PINCH PLASMAS

Laser diagnostics must be optimized for the plasma object of interest. The propagation of a probe beam in a plasma depends on the laser wavelength. Different diagnostics may have specific goals and fields of application. Shadowgraphy, interferometry, schlieren, and Faraday rotation diagnostics are the most common imaging diagnostics for plasmas. They deliver information on density, dynamics, gradients, and magnetic fields in a plasma. The phase shift, absorption, scattering on gradients, and rotation of the plane of polarization of the laser beam in a plasma depend on the wavelength of the radiation. The formulas presented below define these parameters in a plasma.

The critical plasma density n_c defines an electron density threshold for propagation of laser radiation in a plasma:

$$n_c = \frac{\varepsilon_0 m_e}{e^2}\omega^2 = 1.12 \cdot 10^{13}\,\lambda^{-2} \quad (1)$$

with λ measured in cm and n_c in cm^{-3}. The critical density $n_c = 4 \times 10^{21}$ cm^{-3} at 532 nm, and $n_c = 1.6 \times 10^{22}$ cm^{-3} at the fourth harmonic of the neodymium laser (266 nm). For example, a laser-produced plasma can be at the critical density for heating by infrared (IR) light, but transparent to UV probing. The electron plasma density in MA-level Z-pinches is less than critical. In this case, absorption and refraction in the plasma are important for diagnostics. The increment of inverse bremsstrahlung absorption is proportional to λ^2 [Refs. 19 and 20]:

$$\delta = 8.73 \cdot 10^{-30} \cdot \lambda^2 \cdot \frac{n_e^2 \cdot Z \cdot \Lambda}{T_e^{3/2} \cdot \left(1 - \frac{n_e}{n_c}\right)^{1/2}} \quad (2)$$

where λ is the laser beam wavelength in cm, n_e is the electron plasma density in cm^{-3}, T_e is the electron temperature in eV, $\Lambda = 23 - \ln(n_e^{1/2} \cdot Z \cdot T_e^{-3/2})$ is the Coulomb logarithm, Z is the ionic charge, and n_c is the critical density. The total absorption depends exponentially on the increment and the plasma size. The advantage of UV radiation is most pronounced in a plasma with high absorption. At a high plasma density, the IR and optical ranges cannot be used, but transmission in the UV range may still be acceptable. UV diagnostics shows a significant advantage in dense plasma over diagnostics in the IR and visible ranges. However, a plasma object with a low density is transparent to UV radiation. Diagnostics in the IR and optical ranges are preferable for plasmas with electron density < 10^{19} cm^{-3} [Refs. 21 and 22].

Interferometry allows reconstruction of the electron plasma density from the phase shift of a laser beam in a plasma. The phase shift is calculated from the shift of fringes in the interferogram using the formula[23,24]

$$\alpha = 4.49 \cdot 10^{-14}\lambda \int_0^L n_e\, dl, \quad (3)$$

where α is measured in fringes, λ is in cm, and the plasma length L is in cm. Abel inversion is used for reconstruction of the radial electron density in plasma objects with spherical or cylindrical symmetry.

The angle of refraction on the plasma gradient, Θ, can be calculated using the formula[23,24]

$$\Theta = -4.49 \cdot 10^{-14}\lambda^2 \frac{d}{dy} \int n_e(x)\, dx, \quad (4)$$

where the refraction angle is in radians and other quantities are in cm. The refraction angle Θ is proportional to λ^2 and so is smaller by a factor of 16 at a wavelength of 266 nm compared with 1064 nm. Refraction of rays is responsible for the efficiency of schlieren diagnostics. A schlieren effect can be seen in shadowgrams if the acceptance angle of the laser beam path is smaller than the refraction angle.

Faraday rotation of the plane of polarization of the laser beam depends on the magnetic field in the plasma. The angle of rotation of the plane of polarization, β, is given by[23,25]

$$\beta = 2.62 \cdot 10^{-7} \lambda^2 \int_0^L B_x(x) n_e(x) dx, \quad (5)$$

where the rotation angle is in radians, the wavelength λ is in cm, the length L of the plasma slab is in cm, and the electron density n_e is in cm^{-3}. B_x, in gauss, is the projection of the magnetic field onto the direction of the laser beam. The angle of rotation of the plane of polarization is proportional to λ^2, which allows one to measure stronger magnetic fields in the Z-pinch in the UV range. IR Faraday rotation diagnostics are sensitive to magnetic fields in a low-density plasma, but refraction on plasma gradients should be taken into account.[21]

Equations (1)–(5) help to determine optimal wavelengths and diagnostic types, depending on the density, gradient, and size of the plasma object. UV laser probing allows deeper penetration in dense plasmas. UV diagnostics allows investigation of 1 MA Z-pinches even in the stagnation stage. The short wavelength of UV radiation can also provide higher spatial resolution of laser diagnostics owing to the smaller diffraction limit. Laser diagnostics in the IR and optical ranges are more effective for investigation of plasmas of lower density.

III. LASER DIAGNOSTICS AT THE ZEBRA GENERATOR

Z-pinch experiments were performed at the Zebra pulsed power generator.[26] The 1 MA current pulse of the generator has a rising edge of 80 ns (10–90%), with a current prepulse of 200 ns.[27] The impedance of the transmission line is 1.9 Ω. A regime with enhanced load current of 1.5–1.7 MA is available with the use of a load current multiplier.[28] The configuration of the anode–cathode area is shown in Fig. 1(a). Current is measured by three B-dot sensors placed on the anode plate and one sensor located in the stack before the load. The configuration of the anode–cathode area allows installation of apparatus in the vacuum chamber. Optics and apparatus are mounted on damping platforms owing to the strong after-shot shock >200g.

Laser diagnostics can use 5 and 7.5 cm windows spaced at 22.5° increments in the vacuum chamber as shown in Fig. 1(b). The solid arrows in Fig. 1(b) show channels for regular side-on diagnostics, including five-frame shadowgraphy, interferometry, schlieren, and Faraday rotation diagnostics. Details of diagnostics in different experiments are presented in Refs. 15, 29, and 30. The dotted arrows in Fig. 1(b) show probing of the Z-pinch in four directions with 45° shifts.[31] Figure 1(c) shows an end-on laser polarimeter. A laser beam polarized by a polarizer (P) passes vertically through the wire array. A mirror (M) in the hollow cathode reflects the beam to the window in the chamber. A crystal wedge (W) acts as the second polarizer of the polarimeter and splits two orthogonal polarizations.

Mach–Zehnder and shearing air-wedge interferometers[32] are used for plasma density measurements. A differential interferometer is less sensitive by a factor of 5–10 compared with a Mach–Zehnder interferometer. This allows measurements of higher electron density, especially in the UV range.[33]

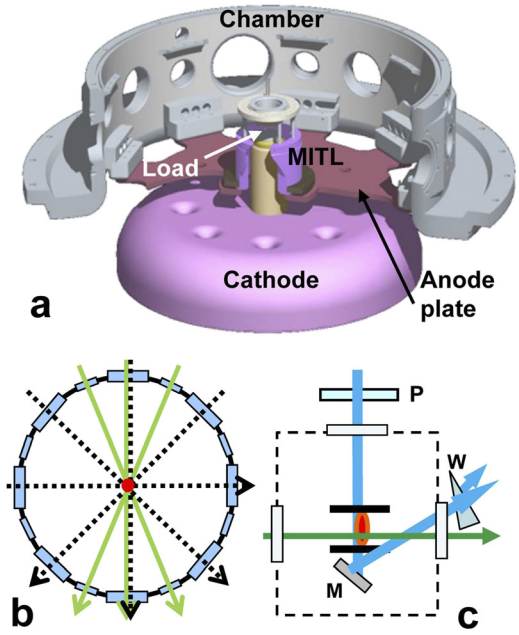

FIG. 1. (a) Configuration of the load zone in the vacuum chamber. (b) Directions of side-on laser probing on the chamber. Solid arrows show regular probing directions, and dotted arrows show probing directions for investigation of pinch asymmetry. (c) End-on laser probing in the vacuum chamber.

A commercial Nd:YAG laser (EKSPLA SL-334) is used for plasma diagnostics. The laser generates pulses of duration of 150 ps at wavelengths 1064, 532, and 266 nm and energies 500, 240, and 80 mJ. A fifth harmonic at 213 nm was generated with an additional β-barium borate (BBO) crystal. Four laser harmonics propagating in one beam path can be used for four-color plasma diagnostics in a single shot.[34]

Three-channel Faraday rotation diagnostics at wavelengths of 532 and 266 nm are used at the Zebra chamber for measurements of magnetic fields.[15,20] The current distribution in the precursor and trailing plasma near the Z-pinch can be reconstructed from the magnetic field profile.[35,36]

The spatial resolution of regular laser diagnostics at the Zebra generator is 12–25 μm, depending on the installed configuration and the magnification of the beam path. A UV laser channel with resolution 4 μm is used for investigation of small-scale perturbations in the Z-pinch.[16] The configurations of the channels and diagnostics are varied according to the goals of specific experiments.

Z-pinches were produced by implosion of cylindrical, planar,[37] and star[38] wire arrays 2 cm tall. Arrays typically consisted of 8–32 wires. Various wire materials such as Al and Au were tested in different shots.

IV. STUDY OF WIRE ARRAYS IN THE ABLATION AND IMPLOSION STAGES

A. Implosion dynamics in wire arrays

Implosion in cylindrical wire arrays was investigated by extreme UV (XUV)[39] and side-on laser diagnostics at 532 nm.[12,15] These diagnostics showed that the plasma implodes in a bubble-like manner. Two-frame shadowgraphy allows detailed investigation of the origin and dynamics of implosion bubbles. Bubbles are blown from the wire material when breaks in the cores arise on wire waists, as seen in Figs. 2(a) and 2(b). The Ampère force accelerates the plasma of the bubbles to velocities of 200–300 km/s over several nanoseconds. The imploding plasma front is inhomogeneous owing to the bubble-like structure. The size of the plasma bubbles decreases as the number of wires increases, but implosion inhomogeneity is seen even in arrays with hundreds of wires.[40] A sketch of an implosion is shown in Fig. 2(d). After implosions in low-wire-number cylindrical arrays and small-diameter arrays, a significant portion of the material remains at the initial position of the wire and implodes later. The schlieren image in Fig. 2(e) shows nonimploded material in an Al 4-wire array. The streams of plasma have the shape of a belt around the initial position of the wire. This shape is formed in the ablation phase, as shown in the sketch of the wire below image (e).

Figures 2(f) and 2(g) show an implosion in a W cylindrical wire array 3 mm in diameter (f) 1.5 ns before and (g) 8 ns after the maximum of the x-ray pulse. A significant part of the material implodes later, resulting in the generation of a long (25–35 ns) x-ray pulse. Secondary implosions are sources of additional x-ray energy in Z-pinches.[9,35] In low-wire-number cylindrical arrays, bubble-like implosions that are asymmetrical and inhomogeneous in space and time result in a longer x-ray pulse and lower power. Implosion inhomogeneity is imprinted on the Z-pinch and seeds sausage and kink instabilities.[29]

Cascade implosion in star wire arrays help to mitigate implosion inhomogeneity.[38,42] The two-frame shadowgram in Figs. 3(a) and 3(b) present a cascade implosion in a 3-ray 12-wire star array. Owing to inductive current division, implosion begins in wires of the outer cylinder. Plasma of the outer array moves and collides with wires in the inner array. During hydrodynamic collision, the moving plasma merges with the plasma of the wire at the next cylinder, and the current switches. Finally, material imploding in the ray is concentrated in a single plasma column, moving to the center. The formation of this plasma column is shown in the two-frame shadowgram in Figs. 3(c) and 3(d). The vertical arrows indicate the center of the Al 3-ray array. The plasma column consists of accumulated material from all wires in the ray. The plasma column is moving to the center of the array. Instabilities arise in the rear edge of

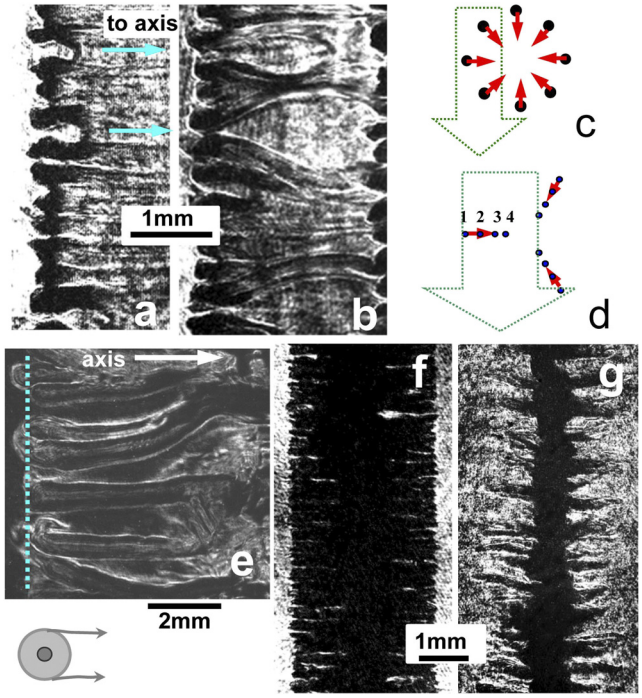

FIG. 2. (a, b) Implosion bubbles in an Al 8-wire cylindrical array taken 22 and 15 ns before the beginning of the x-ray pulse. (c, d) Sketch of implosions in cylindrical and star wire arrays. (e) Schlieren image of nonimploded material in an Al cylindrical 4-wire array 12 ns after the maximum of the x-ray pulse. (f, g) Shadowgrams of a W cylindrical 16-wire array 3 mm in diameter: (f) 1.5 ns before and (g) 8 ns after the maximum of the x-ray pulse.

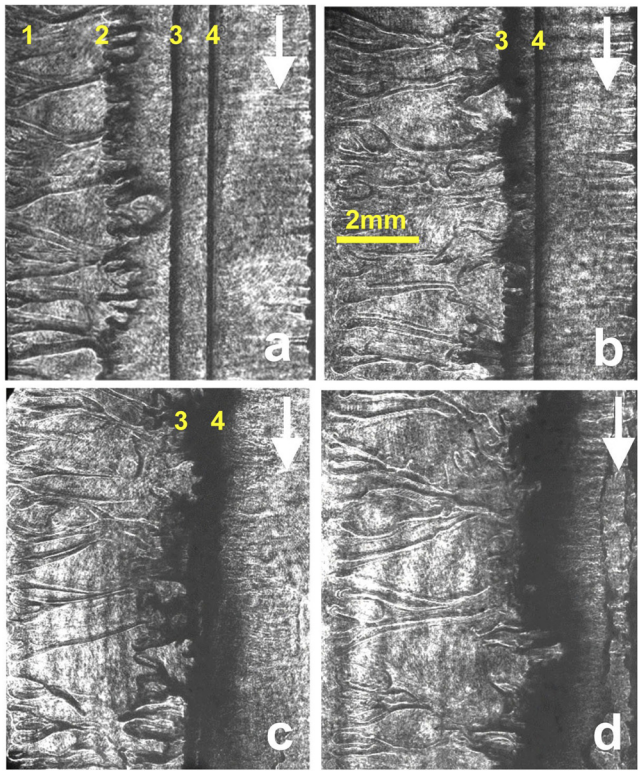

FIG. 3. (a, b) Cascade implosion in an Al 3-ray 12-wire star array. (c, d) Formation of an imploding plasma column on one ray of the 3-ray star array taken in another shot.

the plasma column, while the leading edge of the moving plasma remains uniform. The homogeneity of the imploding plasma explains the high x-ray power radiated by star wire arrays. During implosions in low-wire-number cylindrical arrays, a significant part of the material stays at the initial position of wire and implodes later. A cascade implosion has a more efficient snowplow effect on the material of the wire array. A cascading regime provides generation of short, powerful x-ray pulses in star wire arrays,[38] but the total radiated energy is smaller compared with small-diameter and planar loads.[29,37]

B. Transparent and nontransparent implosion regimes in wire arrays

Cascade implosions in star wire arrays exhibit a hydrodynamic nontransparent regime when the imploding plasma hits the next wire, resulting in plasma mixing.[38,41,42] Transparent propagation of plasma of the external cylinder of wires through the internal cylinder was found in nested arrays consisting of 100–300 wires.[43] Owing to inductive current division, the current in the internal cylinder was only ~4% of the total current. This may decrease the efficiency of the implosion and the generation of the x-ray pulse. Two modes of implosion can be realized in low-wire-number nested arrays at the 1 MA generator.[44] Changing the wire configuration in 8- to 24-wire star arrays allows one to tune the current distribution and provides the transparent regime of implosion in star arrays with "gates."[45] The inductance and current in the inner cylinder was varied by altering the wire lengths. The current in the wire arrays was calculated using formulas from Refs. 46 and 47.

Figure 4 presents a two-color shadowgram of implosion in an Al 3-ray star wire array with double wires ("gates") in the inner circle. The stainless steel gate wires are 4 cm long, whereas the other wires in the rays of the star are of aluminum and 2 cm long. The gate width is 0.5 mm. In this configuration, only a small part of the current flows in the gate wires. The shadowgrams in Figs. 4(a) and 4(b), taken at 532 and 266 nm, respectively, show that the gate wires remain at their initial positions and do not merge with the imploding plasma. At this time, other wires in the star array are imploding to the center and passing through the gates. This plasma front is shown by the arrows in Fig. 4. The imploding plasma has passed through the transparent 0.5 mm gates and keeps moving to the center of the star array. The shadowgram in Fig. 4(a) at a wavelength of 532 nm clearly shows the imploding plasma, while that in Fig. 4(b) at 266 nm reveals the narrow plasma columns of the gate wires.

The current in the wires and return posts, I, was calculated assuming that the magnetic field associated with each wire and return current posts varies as $\mu_0 I/2\pi r$, where r is the radius of the current-carrying region around the wire or post. If the array consists of N_w wires and N_b posts, then the inductance of the wire–post loop is given by[47]

$$L_{ik,jm} = \frac{\mu_0 h}{2\pi} \ln\left(\frac{\mathbf{r}_{im}\mathbf{r}_{jk}}{\mathbf{r}_{ij}\mathbf{r}_{mk}}\right), \tag{6}$$

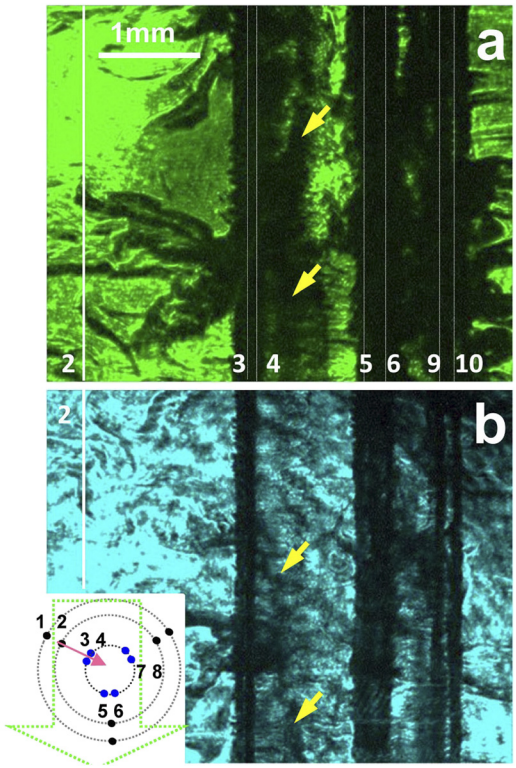

FIG. 4. Shadowgrams of implosion in a 3-ray 12-wire star array with long stainless steel wires in the inner circle. Shadowgrams are taken at the same time at (a) 532 nm and (b) 266 nm. The positions of the wires in shadowgrams are shown in the inset in (b).

where $L_{ik,\,jm}$ is the mutual inductance between the ik and jm contours, the wire indices are i and j, the back-current post indices are k and m, and the distance between wires or posts p and q is r_{pq}. If $i = j$ or $k = m$, then r is the radius of the wire or post. The magnetic flux associated with each current path is

$$\Phi_{ik} = \sum_{j=1}^{N_w} \sum_{m=1}^{N_b} L_{ik,jm}\, I_{jm}. \tag{7}$$

This results in an equation system of size $N_w \times N_b$. The currents are calculated by inverting the matrix of magnetic flux contours. The magnetic field **B** and the **j** × **B** force at the wires are calculated by summation of all the fields from the wires and back posts.[46]

Figure 5(a) shows the currents in the inner cylinders of 3-ray star arrays. The curve represents the results of calculations for stars with different gate widths. The circles represents the results for stars with long gate wires. The diameters of the plasma columns around the gate wires, namely, 0.4 mm (light circles and the curve) and 0.2 mm (dark circles), are taken from shadowgrams of aluminum and stainless steel wires. The current in the inner cylinder is significantly smaller in stars with long stainless steel gate wires, which provide a transparent implosion regime. The plasma columns of stainless steel and

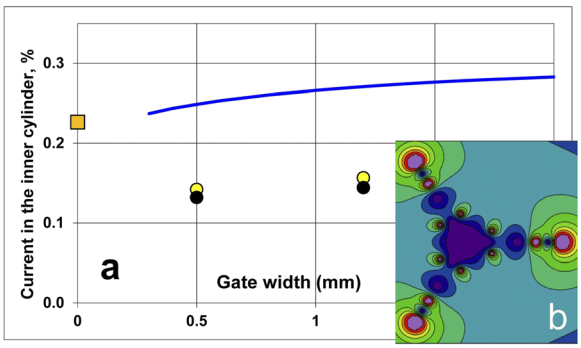

FIG. 5. (a) Currents in the inner cylinders of 3-ray star arrays of diameters 16, 12, and 5 mm as functions of gate width. The curve represents the results of calculations for stars with different gate widths and a regular wire length. The square represents the current in a star with single wires instead of gates. The circles represent stars with long gate wires. The diameters of the plasma columns of the inner wires are 0.4 mm (light circles and the curve) and 0.2 mm (dark circles). (b) Map of the magnetic field in the star array.

tungsten gate wires have smaller diameters compared with those of aluminum wires.

Star loads with gates provide an opportunity to guide ablation and imploding plasma flows in an array. Gates in different configurations of star arrays can be open or closed for imploding plasma flows. This also allows redirection of plasma flows.

C. Nonprecursor ablation and implosion in wire arrays

At the ablation stage, $\mathbf{j} \times \mathbf{B}$ forces move plasma to the center of the array. In cylindrical wire arrays, a precursor arises during the ablation stage.[49] At the end of implosion, the precursor collapses to a dense Z-pinch. The formation of the precursor was observed in nested wire arrays at the Z machine.[50] However, in large 70-mm-diameter nested wire arrays, the precursor plasma was absent owing to plasma from the external cylinder not reaching the axis during the 100 ns implosion time.[50] A rocket model describes ablation of plasma and accumulation in the precursor.[48] However, some configurations of planar, star, and double-cylinder wire arrays allow plasma ablation without the formation of a precursor in the array center.[51] Nonprecursor regimes allow understanding to be obtained of the role of the precursor in Z-pinch formation. The ablating plasma streams can be controlled by changing the magnitude and direction of the initial $\mathbf{j} \times \mathbf{B}$ forces. Planar wire arrays give the simplest examples of manipulation of $\mathbf{j} \times \mathbf{B}$ forces applied to wires.[42] Calculations show that the $\mathbf{j} \times \mathbf{B}$ force applied to wires close to the center is directed away from the center if the gap between the two central wires is wider than the other interwire gaps. The two-frame shadowgram in Figs. 6(a) and 6(b) shows the beginning of the implosion in a linear 6-wire array with a gap between the two central wires that is 50% larger than the interwire gap between the remaining wires. The vertical arrows show the center of the array. Mass ablation is higher on the edge wires. The implosion starts at the edges and moves to

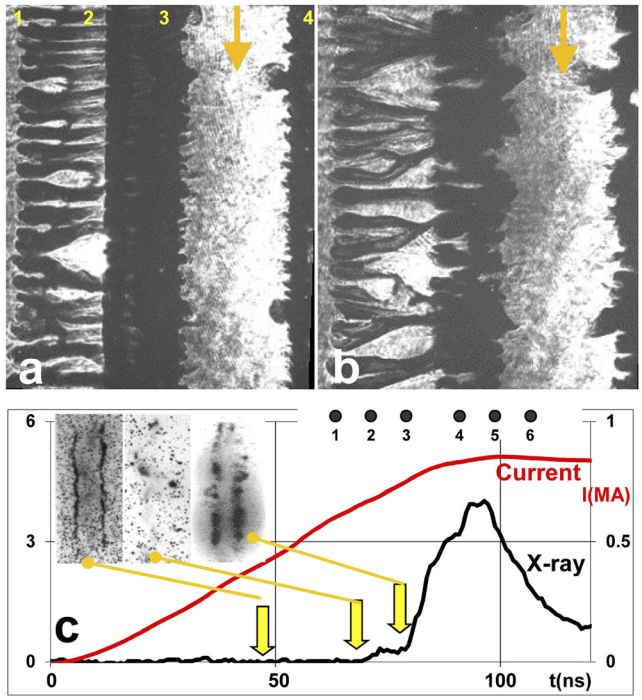

FIG. 6. (a, b) Two-frame shadowgram of implosion in a 12 mm linear array with increased central gap. The shadowgrams were taken 20 and 13 ns before the beginning of the x-ray pulse. The arrows show the axis of the array. (c) X-ray pinhole images with timing.

the center of the array. The central gap in the array is not filled by plasma even in the second frame, 9 ns before the beginning of the x-ray pulse. The $\mathbf{j} \times \mathbf{B}$ force on wires close to the center in Fig. 6(b) is directed away from the center. Finally, two plasma columns collapse to form a dense Z-pinch at the center of the array when the current switches to these columns. An interesting effect in this implosion is the formation of two precursors between wires. Figure 6(c) shows a timing diagram with the current and x-ray pulses. The arrows show the positions of 6 ns frames from the x-ray pinhole camera. Two plasma columns arise in the x-ray image 45 ns after the beginning of the current pulse and disappear in the next frame. New plasma columns arise at the positions of the two wires closest to the center, as can be seen in the last x-ray frame taken immediately before the main x-ray pulse.

Star wire arrays can also implode in the nonprecursor regime. Figures 3(b) and 3(c) show cascade implosion without the formation of a precursor. Star arrays can operate in either regime, depending on the numbers of wires and rays and on the distances between wires. During the nonprecursor implosion regime, a short powerful x-ray pulse is generated in a star array. Calculations of magnetic fields and implosion regimes in stars were performed in Ref. 51.

Double-cylinder cylindrical wire arrays can implode in both regimes at the 1 MA generator. The nonprecursor regime arises in an array with eight wires placed on diameters of

16 and 14 mm, with intercylinder distance Δr = 1 mm. Comparison of an initial global B-field in a double-cylinder array with the local B-field from a neighboring wire shows that the local field is stronger if $\Delta r < R_0/(N-2)$. Here, R_0 and N are the radius and number of wires of the double-cylinder array and $\Delta r \ll R_0$. However, the implosion becomes more complicated in closely spaced nested arrays with Δr = 0.25–0.5 mm.[52] Plasma from wires of the external cylinder ablates and implodes on wires on the internal cylinder. Closely located wires cease to be separated, the currents in the wires merge, and ablating plasma jets from coupled wires create a precursor at the center of the array.

D. Structure of the precursor in cylindrical wire arrays

A stable precursor plasma column arises on the axis of the array during the ablation stage. The arrival of plasma at the axis is due to the formation of a core–corona structure in the wires. The prefilling of the interior of the wire array influences the formation of the main Z-pinch and may reduce instabilities at the imploding plasma front. Precursors in wire arrays have been investigated in detail by side-on laser probing and XUV diagnostics. The XUV diagnostics revealed the structure of the precursor,[52] which may be linked to the temperature distribution in the latter. End-on diagnostics at 532 and 355 nm were used in the ablation stage for investigation of plasma streams.[53] We studied the internal structure of the precursor during the implosion and stagnation stages by UV diagnostics. End-on diagnostics at a wavelength of 266 nm provided data about the imploding plasma streams, the structure of the precursor, and the trailing plasma near the stagnated Z-pinch. The laser diagnostics setup presented in Fig. 1(c) provides both end-on and side-on images of the wire array. A polarimeter was used for investigation of depolarization of the laser beam in the plasma near the Z-pinch. The heights of the loads were decreased to 1 cm to reduce absorption of the laser beam in the Z-pinch plasma.

Figures 7(a)–7(c) show shadowgrams and an interferogram from a shot with an Al 8-wire cylindrical array 12 mm in diameter. Images were taken in the implosion stage 7 ns before the maximum of the generated x-ray pulse. The arrows labeled (1) in Fig. 7(a) indicate the forked structure of the plasma streams near the precursor. An enhanced density on the edge of the precursor is another feature in this shadowgram. Both features are presented in the interferogram in Fig. 7(b). The plasma density in the precursor cannot be reconstructed, owing to the absence of undisturbed reference fringes. However, qualitative interferograms give complementary data owing to the fact that interferometry is not sensitive to temperature and ionization state. Interferometry shows semitransparent areas with a smaller plasma density in the precursor. Fork-like tips of plasma streams can be produced by collisions of plasma with the precursor when the plasma splits on the edge clockwise and counterclockwise. Plasma streams from wires to the precursor to produce dense areas on the precursor column, labeled (2) looking end-on in Fig. 7(b) and side-on in Fig. 7(c).

Plasma at the precursor center is denser compared with the main precursor column, as shown by label (3). The precursor plasma column is supported by the balance between the kinetic

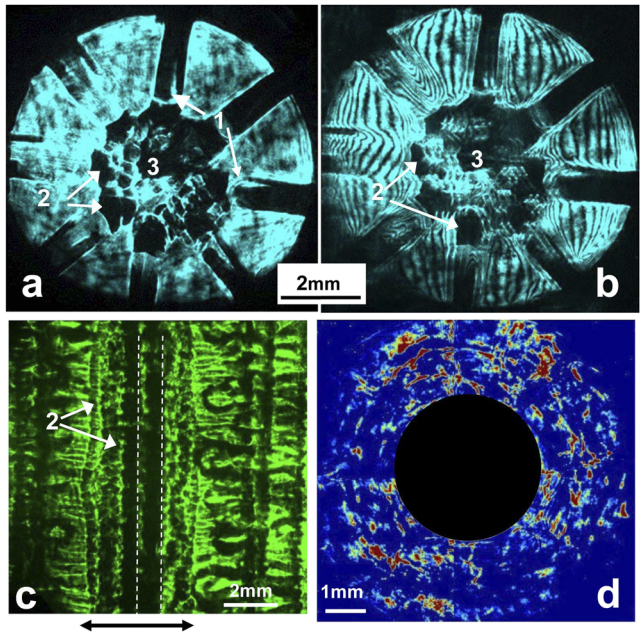

FIG. 7. UV end-on (a) shadowgram and (b) interferogram of the precursor in an Al 8-wire cylindrical array in the implosion stage. (c) Side-on shadowgram of the precursor taken in this shot at the same time. The dashed lines represent two wires in the field of view. (d) Ratio of normalized shadowgram and depolarized image in the peripheral area around the Z-pinch taken from another shot.

pressure of streaming plasma and the thermal pressure of plasma in the precursor.[54] Current in the precursor column[15] may also play a role in this balance.

The precursor plasma column collapses at the end of implosion and produces a dense Z-pinch. Side-on images show nonimploded plasma of lower density. Depolarization of the laser beam in the trailing plasma was studied with the three-channel UV polarimeter shown in Fig. 1(c). The polarimeter takes a shadowgram, a differential interferogram, and an image in depolarized light.

Several factors can affect the polarization of a laser beam in a plasma. An axial magnetic field produces Faraday rotation in a magnetized plasma. Kink instability may generate an axial B-field in the Z-pinch, but this B-field is much smaller than the azimuthal component. In this case, other mechanisms of depolarization in a plasma can play an important role. For example, the Cotton–Mouton effect can induce elliptic polarization if the magnetic field vector is orthogonal to the beam wavevector.[23] Depolarization on plasma gradients orthogonal to the laser beam[55] might also be important. Strong plasma gradients were observed in the imploding plasma and trailing material by side-on diagnostics.

Depolarization of the laser beam can be found if we compare a shadowgram with an image taken in depolarized light. A coefficient of depolarization in the plasma along the radius was calculated as I_D/I_0, where I_0 and I_D are the intensities

of the incident and depolarized beams. This coefficient was calculated from the shadowgram in Fig. 7(a), the depolarized image in Fig. 7(b), and appropriate reference images. A coefficient of depolarization of 0.05–0.15 was measured in different areas of the trailing plasma. Next, we constructed an image using the ratio of the normalized shadowgraphy and depolarized light images to observe objects responsible for depolarization. Figure 7(d) reveals numerous depolarization features in the trailing plasma with characteristic sizes of 25–200 μm. The black disk covers the opaque plasma area near the Z-pinch.

Estimates show that the expected impacts of Faraday rotation and Cotton–Mouton ellipticity are too small to be significant, but depolarization on plasma gradients can explain the observed effect. For a plasma length L = 1 cm and density gradient size l = 30 μm, a depolarization coefficient is in agreement with experimental values. Depolarization may occur on small-scale objects in the trailing plasma seen in side-on shadowgrams.

V. STUDY OF WIRE-ARRAY Z-PINCHES IN THE STAGNATION STAGE

UV laser probing demonstrates a significant advantage compared with laser diagnostics in the optical range. This allows direct investigation of dense plasmas in wire arrays in the ablation, implosion, and stagnation phases.[30,31,33] In this section, plasma dynamics and instabilities are studied in 1 MA wire-array Z-pinches at stagnation.

A. Plasma instabilities in the Z-pinch

Plasma instabilities play a crucial role in the dynamics and radiation capability of Z-pinches. The peak power of a Z-pinch may be limited by the growth of MHD instabilities in the stagnation stage. The stagnated Z-pinch is unstable to both the sausage and kink perturbations. Z-pinch plasma instabilities at the 1 MA pulsed power machine can be studied with UV laser diagnostics.

A setup for UV laser diagnostics at a wavelength of 266 nm was presented in Refs. 16, 18, and 20. A two-component quartz lens in the UV beam path was installed in the vacuum chamber of the Zebra generator and provided spatial resolution of ~4 μm with a field of view of 3 mm. A Z-pinch was probed by two side-on laser beams at wavelengths of 532 and 266 nm, with an angle between channels of 22.5°, as shown by the pictogram in Fig. 8. All laser channels were spatially co-aligned in reference shots on the tip of a removable needle in the center of the wire array.

Strong kink instability and formation of micropinches at the maximum of the x-ray pulse was observed with UV laser diagnostics in Refs. 30 and 56. Shadowgrams at a wavelength of 532 nm typically show a plasma column of trailing plasma. UV shadowgraphy reveals a dense pinch inside the trailing material. Figure 8 presents images of the cylindrical wire-array Z-pinch taken at two wavelengths. The two-frame shadowgram at 532 nm shows a plasma column taken (a) 11 ns and (b) 25 ns after

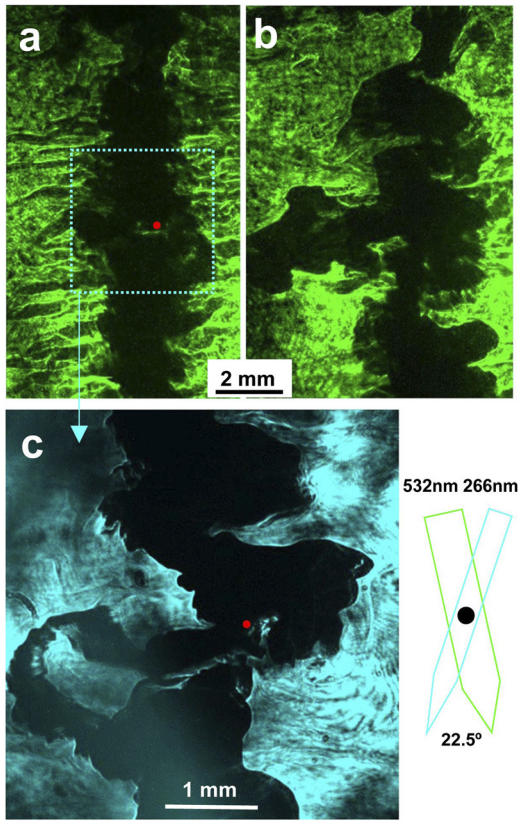

FIG. 8. Shadowgrams of 16-wire, 8-mm-diameter cylindrical Z-pinches, showing the central stagnation column recorded at wavelengths of (a, b) 532 nm and (c) 266 nm. Images are taken (a, c) 11 ns and (b) 35 ns after the maximum of the x-ray pulse. The dots in (a) and (c) show points of spatial co-alignment.

the maximum of the x-ray pulse. The shadowgram (c) at 266 nm presents an area of the rectangle in (a) at the first frame. The UV laser beam penetrates the trailing plasma and reveals the dense pinch with strong kink instability. This dense pinch was hidden inside the column of trailing plasma. The shadowgram (b) at 532 nm shows large growth of the kink 25 ns later. The development of plasma instability is in agreement with 3D MHD Gorgon simulations performed for wire arrays at the Zebra generator.[56]

Figure 8 demonstrates the significant advantage of UV diagnostics compared with diagnostics in the optical range. UV diagnostics at 266 nm allows investigation of different aspects of dense plasma in the 1 MA wire-array Z-pinches. Absorption in the plasma is the main limitation of UV probing. However, it is possible to enhance the intensity of the laser beam on the CCD. A slit can be installed on the CCD camera such that the central area of the Z-pinch is open but illumination of side areas is blocked. The intensity of the laser beam on the slit during a Zebra shot can be increased by a factor of 10–40 compared with the reference shot.

In this way, strong absorption in a dense plasma can be mitigated. The slit protects the CCD camera from damage in the

side areas with low absorption. High laser energy and narrowband spectral filtering are important to distinguish the UV laser signal from plasma self-emission.

Dense Z-pinches studied with enhanced laser intensity using high-resolution UV diagnostics. Figure 9(a) shows a shadowgram of the central area of the pinch of an Al 18-wire star array. Figures 9(b) and 9(c) present magnified areas from the shadowgram. Density perturbations with a characteristic scale of 10–20 μm are seen in the plasma on high magnification. Small-scale density perturbations were also observed in the precursor plasma[56] and in the pinch at the end of the stagnation stage.[30] Another type of plasma instability in wire-array Z-pinches is presented in Ref. 30. Modulation with a period of 100–300 μm has been observed on the edges of the pinch.

B. Plasma dynamics and asymmetry of wire-array Z-pinches

A dense Z-pinch is typically surrounded by nonimploded trailing material. X-ray and laser diagnostics of Z-pinches often collect data in one spatial direction. Data from diagnostics may vary in different azimuthal directions if the trailing plasma is asymmetrical. Understanding the spatial profile of the Z-pinch and the trailing plasma at stagnation is important for interpretation of diagnostic data. Asymmetry of the trailing plasma is linked to the implosion features of the wire array.

The high penetration capability of UV diagnostics allows investigation of plasma dynamics in Z-pinches in the stagnation stage. Two-frame UV shadowgraphy was used to study plasma motion in a stagnated pinch. The laser pulse was split into two pulses with orthogonal polarizations.[16] These pulses propagated through the Z-pinch plasma in one direction with a delay of 2.7–7 ns. A crystal wedge split orthogonal polarizations after the pulses had passed the pinch. The two laser pulses propagated in one beam path. Depolarization in the beam path was minimized by using appropriate dielectric mirrors. Polarizers separated the two pulses with different delays onto two CCD cameras. An air-wedge differential interferometer was used for measurements of plasma density.

Figure 10 presents images of a cylindrical 8-wire array, 2 mm in diameter, taken by laser and x-ray diagnostics. The images (a) and (b) are two frames of UV shadowgraphy taken at the same position with 5 ns between frames. The shadowgram (c) at 532 nm is timed to the first UV frame. An area of the UV image (c) is shown by the dashed rectangle. All laser images were aligned on the tip of the needle in the reference shot before the Zebra shot. The dense Z-pinch is hidden by trailing plasma in the image (c) at 532 nm; however, it can seen at 266 nm. The two frames show fast plasma dynamics in the pinch in the stagnation stage. The images (a) and (c) are recorded at the maximum of the 30 ns x-ray pulse radiated by the small-diameter load. The arrows and rectangles mark features with fast plasma dynamics. The arrows in images (a) and (b) show the

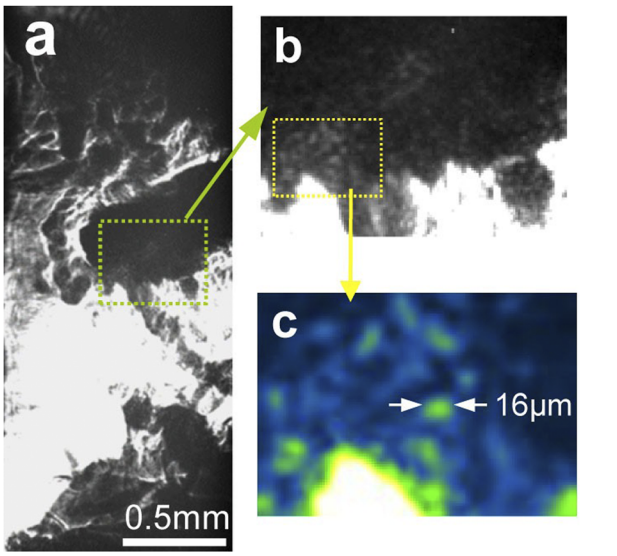

FIG. 9. (a, b) Shadowgram of the Z-pinch in an Al 3-ray star array taken with enhanced intensity through a slit at the maximum of the x-ray pulse. (b, c) Magnified images from this shadowgram.

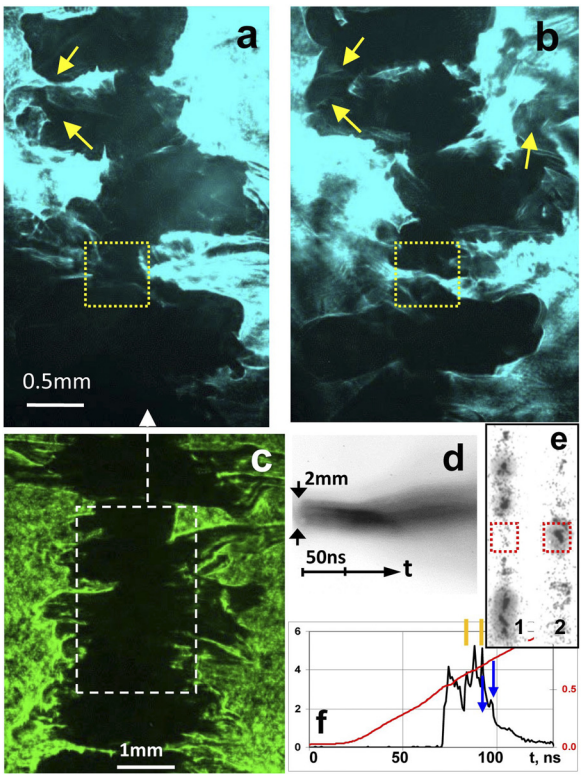

FIG. 10. (a, b) Two-frame UV shadowgram of a 2-mm-diameter, 8-wire array. The frames are 3 ns long with 5 ns between frames. (c) Shadowgram at 532 nm taken at 22.5° to images (a) and (b) and timed to image (a). The shadowgrams (a) and (c) were taken at the maximum of the x-ray pulse. (d) Optical streak camera image showing emission through stagnation. (e) X-ray images from a time-gated pinhole camera. (f) Timing diagram with current (red line), x-ray pulse (black), UV frames (arrows), and x-ray frames (strips).

formation of plasma jets, which move from one bulge to another and create a plasma bridge. This plasma bridge may work like an additional path for current, which can bypass the main current flowing in the neck of the pinch. Two-frame diagnostics shows that plasma jets move with a velocity >100 km/s.[16] This velocity is comparable to the implosion velocity in the 1 MA Z-pinch.

The dotted squares in the two-frame UV shadowgram in Figs. 10(a) and 10(b) show a neck in the first frame and a gap on the pinch in the second frame. We can link this dynamics to the fast collapse and formation of a micropinch and a hot spot on the neck. The collapse results in explosion of the hot spot and the formation of a gap on the pinch where plasma is absent. Optical and x-ray images from this shot deliver additional data. The image in Fig. 10(d) from the optical streak camera shows that a 2 mm load implodes to the pinch with almost the same diameter. The stagnation stage with bright radiation in this image lasts ~40 ns. The two x-ray frames in Fig. 10(e) with 5 ns between frames were filtered for photon energy > 3 keV. The frames show the evolution of bright spots on the Z-pinch. The spatial resolution of the pinhole images is 0.25 mm. A timing diagram for the laser and x-ray frames is shown in Fig. 10(f). The dotted squares in the x-ray images show radiation from the neck plasma in frame (e-1) and a bright spot in frame (e-2) formed by the collapse of the micropinch. Fast expansion of the plasma after the collapse produces the gap in the Z-pinch seen in the shadowgram (b).

Plasma instabilities and inhomogeneous implosion in an asymmetrical wire array may result in the formation of an asymmetrical Z-pinch. We studied spatial profiles of Z-pinches using four-channel shadowgraphy at a wavelength of 266 nm. Three beam splitters split the input laser beam into four channels with equal energy and delay, spaced at 45° increments as shown in Fig. 1(b). The difference in delays in the channels was ~0.1 ns. Four images of the plasma were transferred to appropriate CCD cameras through four three-lens beam paths with the same lenses, magnification, and acceptance angle of 2.8°.[31] A reference laser image was recorded in every channel before the main shot. We studied cylindrical loads and linear and star wire arrays. Figure 11 shows four shadowgrams of a Z-pinch produced by a linear 8-wire array taken in the stagnation stage. A zero probing angle in Fig. 11(a) corresponds to propagation of the laser beam along the line of wires in the planar arrays. The shadowgrams from the four directions in Fig. 11 are very different. Image (a) reveals a narrow homogeneous pinch with 0.5–1 mm plasma jets orthogonal to the wire array. The shadowgram (c) is taken in the orthogonal direction to image (a). One feature of the image is the presence of finger-like nonimploded plasma near the edges of the linear array. The trailing plasma has necks and bulges with vertical periods of 2–3 mm. Most of the trailing plasma stays in the plane of the line of wires in the stagnation stage owing to the "planar" nature of the implosion. Wide trailing plasma can absorb x-ray radiation in one direction, which results in asymmetrical radiation of the Z-pinch.[57]

Cylindrical and star wire-array Z-pinches exhibit less asymmetry of the trailing plasma. Inhomogeneous implosion can seed asymmetrical kink instabilities in cylindrical wire arrays. Cascade implosion in star arrays forms a Z-pinch without kink instability and with a small amount of trailing material.

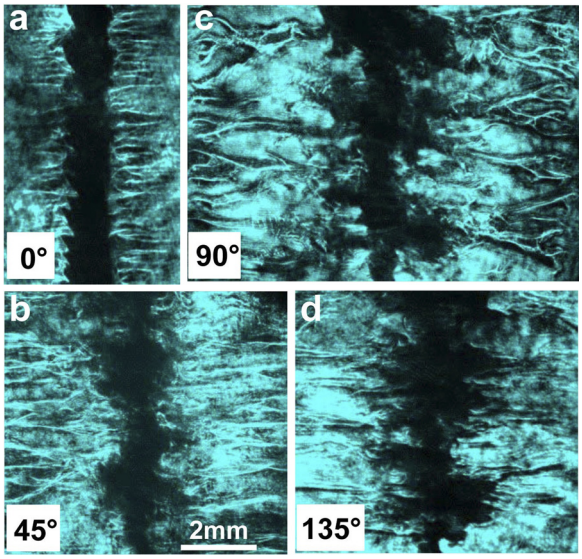

FIG. 11. Shadowgrams of a Z-pinch in an Al planar 10-wire array taken from different angles 4 ns after the maximum of the x-ray pulse.

Assymetry of the trailing plasma is important for laser and optical diagnostics when cylindrical symmetry of the plasma is assumed for Abel inversion. Asymmetry of the Z-pinch plasma can make interpretation of data from laser and x-ray diagnostics difficult if these are taken from different azimuthal directions.

C. "Bright spots" in wire-array Z-pinches

Small strongly radiating bright (hot) spots are observed in all kinds of Z-pinches, including wire arrays, gas puffs, plasma foci, and X-pinches. Hot spots radiate continuum spectrum in the keV range that is a signature of the high plasma density. The electron plasma density in X-pinches is in the range of 10^{22}–10^{23} cm^{-3} [Ref. 58]. The electron temperature in hot spots varies from 1 to 3 keV.[59] The hot spot that occurs in the cross-over area of the wires in an X-pinch is well investigated. This hot spot radiates during ~100 ps in the keV spectral range with a dense core of size 1–5 μm.[58] In other types of Z-pinch, hot spots arise on the pinch spontaneously in space and time. We used a high-dynamic-range x-ray streak camera coupled with UV laser diagnostics to study hot spots in wire-array Z-pinches.

Two Au and CsI photocathodes of the streak camera recorded images in the energy ranges of 50–200 eV and >0.8 keV, respectively.[60] The temporal resolutions of the streak camera were 100 and 10 ps in the 50 and 5 ns sweep ranges, respectively. The streak camera was triggered by the 150 ps UV laser pulse, and the main probing UV pulses were delayed. This provided accurate timing of laser frames to the streak image. The spatial resolution of the photocathode with a 40 μm slit was 100 μm. X-ray and laser diagnostics were

co-aligned with an accuracy of ~0.5 mm. UV laser diagnostics operated either as two-frame shadowgraphy or as a three-channel polarimeter with a field of view of 8 mm × 8 mm and a spatial resolution of 15 μm. The experiments were performed with compact cylindrical and planar wire arrays. These loads generate numerous bright spots in every shot.

Figure 12 presents (a) a streak image and (b) a shadowgram taken in a shot with a cylindrical wire array 3 mm in diameter. The streak image reveals short-lasting, compact, powerful sources of x-ray radiation. Images (a) and (b) are vertically co-aligned with equal spatial magnification. The vertical arrow in (a) marks the temporal position of the UV shadowgram. A width of the arrow line fits a duration of the laser pulse. A dashed arrow shows that a hot spot in the streak image coincides in time and space with a micropinch on the Z-pinch. This UV image of the micropinch is similar to images of micropinches in X-pinches taken with x-ray radiography. Figure 12 confirms that hot spots in wire-array Z-pinches have a micropinch origin. Micropinches produce small, hot, and dense plasma objects in x-ray images (hot spots) during the collapse. The lifespan of hot spots in streak images is in the range of 0.6–2 ns. Micropinches generate a continuum spectrum in the keV spectral range. The axial size is 0.3–0.7 mm. Micropinches arise in necks on the Z-pinch in the stagnation stage. Necks represent an MHD instability in plasmas and can exist for >10 ns in small-diameter wire-array Z-pinches. One hot spot can radiate 1–2% of the total energy of the Z-pinch. A shot with a small-diameter cylindrical wire array produces 5–10 hot spots with a contribution of 10–20% to the total radiated energy. A detailed analysis of the dynamics of micropinches is presented in Ref. 60.

D. Magnetic fields and current distributions in the Z-pinch and trailing plasma

Current distribution in the Z-pinch plasma is crucial for implosion and stagnation dynamics. Current in the trailing plasma decreases the efficiency of the Z-pinch implosion and the generation of x-ray radiation. Current plays an important role in the formation of instabilities and micropinches. For example, "disappearance" of current from the neck of a Z-pinch was reported in Ref. 61. We used Faraday rotation diagnostics to measure magnetic fields and study the current distribution in wire-array Z-pinches.[35,36,61] Faraday rotation diagnostics can provide useful information about current distributions even if plasma density cannot be reconstructed.[62] Figure 13 presents (a) a shadowgram and (b) a Faraday image from a shot with a cylindrical wire array 8 mm in diameter. An optical schematic of UV side-on Faraday rotation diagnostics is presented in Ref. 35. A Z-pinch is located between two polarizers. The first polarizer creates a linearly polarized laser beam with a contrast of 10^5. A crystal wedge acts as the second polarizer. This crystal wedge is mismatched to the first polarizer with a small angle β_0 = 2–5°. In this case, background illumination of the CCD in the Faraday channel allows identification of magnetic field directions. Positive and negative rotation of the plane of polarization result in lightening and darkening in the Faraday image. Comparison of the shadowgram and Faraday image provides interesting qualitative data about current in the Z-pinch.

The Faraday image in Fig. 13(b) demonstrates general lightening on the right side of the image and darkening on the left due to the current and magnetic field. Analysis of the details of light and dark areas helps visualize the current path in the pinch. The dashed curve in image (b) shows the main current path. This path mostly coincides with the center of the dense pinch in image (a). However, additional paths are seen in the Faraday image. The dotted curves mark dark–light areas in the trailing plasma near the pinch. Part of the current switches from the kink pinch with a higher inductance to the trailing plasma. Quantitative measurements show that 20–30% of the current can split from the main current.[35]

Faraday rotation diagnostics allows reconstruction of magnetic fields in a plasma if the rotation angle and plasma

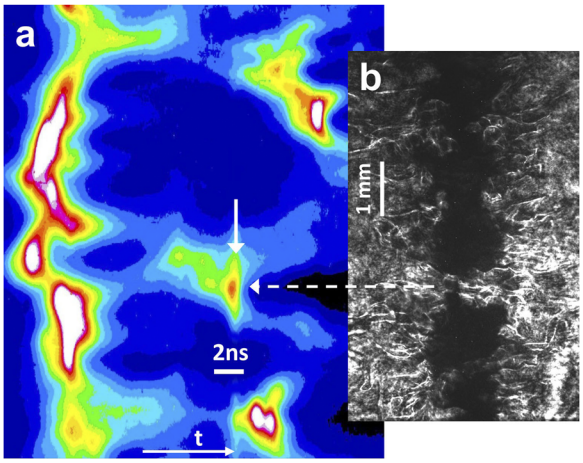

FIG. 12. (a) Images from an x-ray streak camera and (b) UV shadowgram recorded in a shot with an Al 8-wire cylindrical array 3 mm in diameter. The vertical arrow in (a) shows the temporal position of (b).

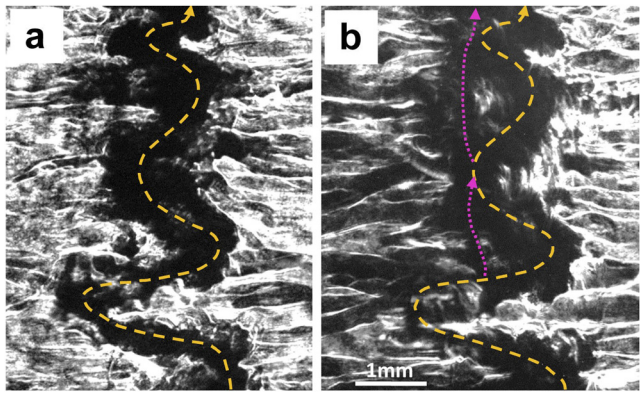

FIG. 13. (a) UV shadowgram and (b) complementary Faraday image taken in a shot with an Al 8-wire cylindrical array, 8 mm in diameter, at the maximum of the x-ray pulse.

electron density are measured.[23] The radial profile of the electron density can be calculated in a plasma with cylindrical or spherical symmetry using Abel inversion:

$$N_e(r) = -K\int_r^{R_0} \frac{d\varphi(y)}{dy}\frac{dy}{\sqrt{y^2-r^2}}, \quad (8)$$

where $\varphi(y)$ is the phase shift, R_0 is the radius of the plasma column, y is the distance from the axis, $K = 2e^2\lambda/(mc^2)$ in Gaussian units, λ is the wavelength, e and m are the electron charge and mass, and c is the speed of light. The rotation angle of the plane of polarization, β, is calculated from the shadowgram, Faraday image, and their reference images as described in Ref. 33. The profile of the magnetic field $B(r)$ can also be reconstructed using Abel inversion:

$$\frac{B(r)N_e(r)}{r} = \frac{2}{\pi\kappa}\int_y^{R_0}\frac{d}{dy}\left(\frac{\beta(y)}{y}\right)\frac{dy}{\sqrt{y^2-r^2}}, \quad (9)$$

where $\kappa = 2e^3\lambda^2/(\pi m^2c^4)$ in Gaussian units. The electron density $n_e(r)$ is calculated using Eq. (8). Quantitative analysis of magnetic fields can reconstruct the distribution of current in the Z-pinch.

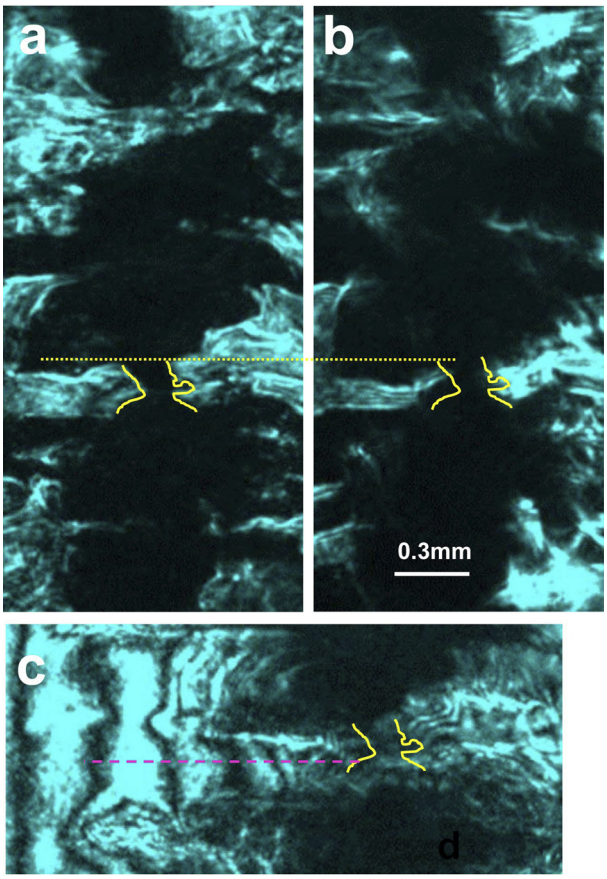

FIG. 14. (a) UV shadowgram, (b) Faraday image, and (c) interferogram taken in a shot with an Al 8-wire cylindrical array, 8 mm in diameter, at the maximum of the x-ray pulse.

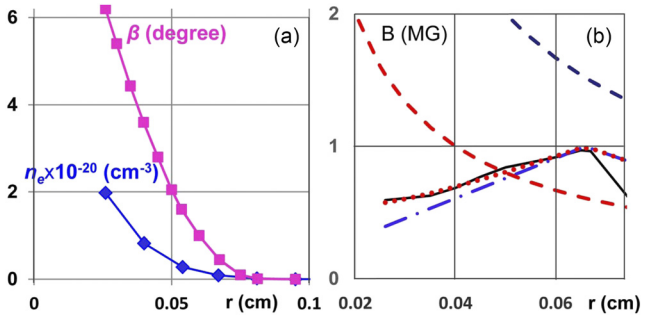

FIG. 15. (a) Faraday rotation angle (squares) and plasma electron density (diamonds). (b) Reconstructed magnetic field (solid curve), magnetic field of current flowing in the 0.2 mm neck only (dashed curves), a B-field calculated for a constant current density (dashed-dotted curve), and with enhanced current density in the neck (dotted curve).

Figure 14(a) presents a shadowgram, Fig. 14(b) a Faraday image, and Fig. 14(c) an interferogram at 266 nm taken in a shot with a cylindrical array, 8 mm in diameter. The current near the thin neck was analyzed in the direction of the horizontal dashed line in (c). The electron plasma density $n_e(r)$ was calculated from the phase shift in the differential interferogram (c) using the Abel inversion, Eq. (8). The radial profiles of the electron plasma density and Faraday rotation angle are presented in Fig. 15(a). Figure 1 (b) shows the magnetic field $B(r)$ calculated using Eq. (9) and magnetic fields calculated with different models of the current distribution.[36] The dashed curves show the magnetic fields when 20% and 50% of current flows in a neck of diameter 0.2 mm. These magnetic fields differ from the experimental magnetic field shown by the solid curve. This means that current flows in a wide area, including the trailing plasma. The dashed-dotted curve shows the magnetic field of current $I = 0.3$ MA with a constant current density profile and a plasma diameter of 1.3 mm. The dotted curve shows a magnetic field with the same total current but in the case where the current density is enhanced in the neck by a factor of 5. This current distribution is in better agreement with the experimental curve. However, the current in a radius of 1.3 mm includes only ~70% of the current measured by the B-dots. This discrepancy may be explained by the fact that current also flows in the low-density plasma at larger radii. A low-density plasma is not seen in the interferogram at a wavelength of 266 nm.

VI. CONCLUSIONS

Wire arrays have been studied at the 1 MA Zebra pulsed power generator using laser and x-ray diagnostics. Laser diagnostics at different wavelengths allow investigation of Z-pinch plasmas in all stages. Interferometry, shadowgraphy, schlieren, and Faraday diagnostics deliver data about plasma dynamics, density, gradients, and magnetic fields. Multiframe diagnostics shows plasma dynamics in wire arrays. The imploding plasma in low-wire-number cylindrical arrays has a bubble-like structure. Cascading in star wire arrays provides a smooth implosion plasma front and generation of a short

powerful x-ray pulse. Some configurations of wire arrays exhibit ablation and implosion in the nonprecursor regime. Star loads with gates provide an opportunity for guiding ablation and imploding plasma flows.

UV laser diagnostics allows deep penetration into the dense Z-pinch plasma at the 1 MA generator. End-on UV probing reveals the structure of the precursor, with increased density at the edges of the plasma column. The dense pinch at stagnation is hidden in the trailing plasma. This trailing plasma is not transparent to diagnostics in the visible range. However, UV diagnostics shows strong MHD kink and sausage instabilities, and medium and small-scale instabilities in Z-pinch plasmas in the implosion and stagnation stages. Small-scale plasma perturbations with a characteristic size of 10–50 μm are seen in the high-resolution UV channel. Electron plasma densities of (1–3) × 10^{20} cm^{-3} were measured in the Z-pinch by interferometry at 266 nm.

UV probing of the Z-pinch in four directions reveals asymmetrical plasmas in some types of wire array. The asymmetry of the Z-pinch plasma should be taken into account in interpretation of data from plasma diagnostics. Two-frame UV diagnostics visualizes fast plasma motion in the dense Z-pinch at stagnation. This means that the stagnation stage is not static but may involve reconfiguration of plasma and the formation of breaks on the pinch. UV imaging diagnostics coupled with x-ray streak camera images shows the formation of a hot spot after the collapse of a micropinch on the neck of the Z-pinch. Hot spots generate a significant part of the x-ray energy in some types of wire array.

Faraday rotation diagnostics reveals the magnetic fields and the current distribution in the precursor and the dense Z-pinch. Redistribution of current into the trailing material near the pinch is seen during the stagnation stage. In the vicinity of the neck, current flows through a wide area, including the trailing plasma. End-on polarimetry reveals numerous features with characteristic sizes of 25-200 μm in the trailing plasma.

Deep UV diagnostics at a wavelength of 213 nm provides better probing capability in dense Z-pinch plasmas than diagnostics at 266 nm. Multicolor laser diagnostics can show plasma in a wide range of densities in a single laser shot. Further development of laser diagnostics will facilitate better understanding of the complicated physics of dense Z-pinches.

ACKNOWLEDGMENTS

The authors thank the team of the Nevada Terawatt Facility at UNR for their help in experiments at the Zebra generator. This work was supported by DOE/NNSA Grant DE-NA 0002075 and DOE Grant DE-SC0016500.

REFERENCES

[1]D. D. Ryutov, M. S. Derzon, and M. K. Matzen, "The physics of fast Z-pinches," Rev. Mod. Phys. **72**(1), 167–223 (2000).

[2]M. G. Haines, Plasma Phys. Control. Fusion **53**, 093001 (2011).

[3]C. Deeney, R. Douglas, R. B. Spielman, T. J. Nash, D. L. Peterson, P. L'Eplattenier, G. A. Chandler, J. F. Seaman, and K. W. Struve, "Enhancement of x-ray power of Z-pinch using nested-wire arrays," Phys. Rev. Lett. **81**(22), 4883–4886 (1998).

[4]R. B. Spielman, C. Deeney, G. A. Chandler, M. R. Douglas, D. L. Fehl, M. K. Matzen, D. H. McDaniel, T. J. Nash, J. L. Porter, T. W. L. Sanford, J. F. Seaman, W. A. Stygar, K. W. Struve, S. P. Breeze, J. S. McGurn, J. A. Torres, D. M. Zagar, T. L. Gilliland, D. O. Jobe, J. L. McKenney, R. C. Mock, M. Vagras, T. Wagoner, and D. L. Peterson, Phys. Plasmas **5**, 2105 (1998).

[5]B. A. Remington, R. P. Drake, and D. D. Ryutov, Rev. Mod. Phys. **78**, 755 (2006).

[6]S. V. Lebedev, F. N. Beg, S. N. Bland, J. P. Chittenden, A. E. Dangor, M. G. Haines, S. A. Pikuz, and T. A. Shelkovenko, Phys. Rev. Lett. **85**, 98 (2000).

[7]S. N. Bland, S. V. Lebedev, J. P. Chittenden, C. Jennings, and M. G. Haines, Phys. Plasmas **4**, 1100 (2003).

[8]V. V. Ivanov, V. I. Sotnikov, V. L. Kantsyrev, V. I. Sotnikov, D. A. Fedin, A. L. Astanovitskiy, B. Le Galloudec, V. Nalajala, I. Shrestha, T. E. Cowan, B. Jones, C. A. Coverdale, C. Deeney, and P. D. LePell, "Investigation of regimes of wire array implosion on the 1-MA Zebra accelerator," Phys. Plasmas **13**(12), 012704 (2006).

[9]S. V. Lebedev, F. N. Beg, S. N. Bland, J. P. Chittenden, A. E. Dangor, and M. G. Haines, Phys. Plasmas **5**, 2293 (2002).

[10]N. R. Pereira and J. Davis, J. Appl. Phys. **64**, R1 (1988).

[11]M. E. Cuneo, E. M. Wasiman, S. V. Lebedev, J. P. Chittenden, W. A. Stygar, G. A. Chandler, R. A. Vesey, E. P. Yu, T. J. Nash, D. E. Bliss, G. S. Sarkisov, T. C. Wagoner, G. R. Bennett, D. B. Sinars, J. L. Porter, W. W. Simpson, L. E. Ruggles, D. F. Wenger, C. J. Garasi, B. V. Oliver, R. A. Aragon, W. E. Fowler, M. C. Hettrick, G. C. Idzorek, D. Johnson, K. Keller, S. E. Lazier, J. S. McGurn, T. A. Mehlhorn, T. Moore, D. S. Nielsen, J. Pyle, S. Speas, K. W. Struve, and J. A. Torres, Phys. Rev. E **71**, 046406 (2005).

[12]V. V. Ivanov, V. I. Sotnikov, G. S. Sarkisov, T. E. Cowan, S. N. Bland, B. Jones, C. A. Coverdale, C. Deeney, P. J. Laca, A. L. Astanovitskiy, and A. Haboub, "Dynamics of mass transport and magnetic fields in low-wire-number-array Z pinches," Phys. Rev. Lett. **97**, 125001 (2006).

[13]V. V. Ivanov, V. I. Sotnikov, G. S. Sarkisov, A. L. Astanovitskiy, P. J. Laca, T. E. Cowan, B. Jones, C. Deeney, B. V. Oliver, T. A. Mehlhorn, and J. N. Leboeuf, "Experimental study of the dynamics of large- and small-scale structures in the plasma column of wire array Z-pinches," IEEE Trans. Plasma Sci. **35**(4), 1170–1177 (2007).

[14]V. I. Sotnikov, V. V. Ivanov, T. E. Cowan, J. N. Leboeuf, B. V. Oliver, C. A. Coverdale, B. M. Jones, C. Deeney, T. A. Mehlhorn, G. S. Sarkisov, and P. D. LePell, "Investigation of electromagnetic flute mode instability in a high beta Z-pinch plasma," IEEE Trans. Plasma Sci. **34**, 2239 (2006).

[15]V. V. Ivanov, G. S. Sarkisov, P. Laca, V. I. Sotnikov, V. L. Kantsyrev, B. Jones, C. A. Coverdale, P. D. LePell, C. Deeney, K. W. Struve *et al.*, "Investigation of magnetic fields in 1-MA wire arrays and X-pinches," IEEE Trans. Plasma Sci. **34**(5), 2247–2250 (2006).

[16]S. D. Altemara, D. Papp, V. V. Ivanov, A. A. Anderson, A. A. Astanovitskiy, and V. Nalajala, "High-resolution UV laser diagnostics on the 1-MA Zebra generator," IEEE Trans. Plasma Sci. **40**(12), 3378–3383 (2012).

[17]Z. Wang, J. L. Yang, N. Ding, I. N. Frolov, R. K. Xu, Z. H. Li, E. V. Grabovsky, G. M. Oleinik, C. Ning, L. B. Li, I. Yu. Porofeev, V. P. Smirnov, Z. P. Xu, J. M. Ning, and Y. H. Zhong, "UV laser probing of the imploding wire-array plasmas on the Angara 5-1 facility," IEEE Trans. Plasma Sci. **36**, 174–180 (2008).

[18]V. V. Ivanov, S. D. Altemara, A. L. Astanovitskiy, G. S. Sarkisov, A. Haboub, D. Papp, and J. M. Kindel, "Development of UV laser probing diagnostics for 1-MA Z-pinches," IEEE Trans. Plasma Sci. **38**(4), 574–580 (2010).

[19]T. W. Johnson and J. M. Dawson, "Correct values for high-frequency power absorption by inverse bremsstrahlung in plasma," Phys. Fluids **16**(5), 722 (1973).

[20]V. V. Ivanov, A. A. Anderson, D. Papp, B. R. Talbot, J. P. Chittenden, N. Niasse, and I. A. Begishev, "UV laser-probing diagnostics for the dense Z pinch," IEEE Trans. Plasma Sci. **42**(5), 1153–1161 (2014).

[21]G. F. Swadling, S. V. Lebedev, G. N. Hall, S. Patankar, N. H. Stewart, R. A. Smith, A. J. Harvey-Thompson, G. C. Burdiak, P. de Grouchy, J. Skidmore *et al.*, Rev. Sci. Instrum. **85**, 11E502 (2014).

[22]V. V. Ivanov, E. S. McKee, B. D. Hammel, T. W. Darling, K. J. Swanson, and A. M. Covington, "Infrared laser diagnostics for deuterium gas puff Z-pinches," Rev. Sci. Instrum. **88**, 076111 (2017).

[23]I. H. Hutchinson, Principles of Plasma Diagnostics (Cambridge University Press, Cambridge, New York, 1987).
[24]G. S. Sarkisov, "Simulation of laser beam propagation through an axisymmetric dense plasma," Quantum Electron. **26**(9), 799–805 (1996).
[25]J. A. Stamper and B. H. Ripin, "Faraday-rotation measurements of megagauss magnetic fields in laser-produced plasma," Phys. Rev. Lett. **34**(3), 138–141 (1975).
[26]B. S. Bauer, V. L. Kantsyrev, F. Winterberg, A. S. Shlyaptseva, R. C. Mancini, H. Li, and A. Oxner, in *Proceedings of the Fourth International Conference on Dense Z-pinches*, Vancouver, Canada, 1997 [AIP Conf. Proc. **409**, 153, 1997].
[27]G. S. Sarkisov, S. E. Rosenthal, K. W. Struve, V. V. Ivanov, T. E. Cowan, A. Astanovitskiy, and A. Haboub, Phys. Plasmas **14**, 052704 (2007).
[28]A. Chuvatin, V. L. Kantsyrev, L. I. Rudakov, M. E. Cuneo, A. L. Astanovitskiy *et al.*, Phys. Rev. Spec. Top.–Accel. Beams **13**, 010401 (2010).
[29]V. V. Ivanov, V. I. Sotnikov, J. M. Kindel, P. Hakel, R. C. Mancini, A. L. Astanovitskiy, A. Haboub, S. D. Altemara, A. P. Shevelko, E. D. Kazakov, and P. V. Sasorov, Phys. Rev. E **79**, 056404 (2009).
[30]V. V. Ivanov, J. P. Chittenden, R. C. Mancini, D. Papp, N. Niasse, S. D. Altemara, and A. A. Anderson, "Investigation of plasma instabilities in the stagnated Z pinch," Phys. Rev. E **86**, 046403 (2012).
[31]V. V. Ivanov and A. A. Anderson, High Energy Density Phys. **20**, 570 (2016).
[32]G. S. Sarkisov, Instrum. Exp. Tech. **39**, 727 (1996).
[33]A. A. Anderson, V. V. Ivanov, A. L. Astanovitskiy, D. Papp, P. P. Wiewior, and O. Chalyy, "Study of ablation and implosion stages in wire arrays using coupled UV and x-ray probing diagnostics," Phys. Plasmas **22**, 112702 (2015).
[34]V. V. Ivanov, A. A. Anderson, and I. A. Begishev, "Four-color laser diagnostics for Z-pinches and laser produced plasma," Appl. Opt. **55**, 498 (2016).
[35]V. V. Ivanov, A. A. Anderson, D. Papp, A. L. Astanovitskiy, B. Talbot, J. P. Chittenden, and N. Niasse, "Current redistribution and generation of kinetic energy in the stagnated Z pinch," Phys. Rev. E **88**, 013108 (2013).
[36]V. V. Ivanov, A. A. Anderson, D. Papp, A. L. Astanovitskiy, V. Nalajala, and O. Dmitriev, "Study of magnetic fields and current in the Z pinch at stagnation," Phys. Plasmas **22**, 092710 (2015).
[37]V. L. Kantsyrev, L. I. Rudakov, A. S. Safronova, A. L. Velikovich, V. V. Ivanov, C. A. Coverdale, B. Jones, P. D. LePell, D. J. Ampleford, C. Deeney, A. S. Chuvatin, K. Williamson, I. Shrestha, N. Quart, M. F. Yilmaz, G. Osborne, A. Haboub, S. Batie, A. Astanovitskiy, B. LeGalloudec, V. Nalajala, W. McDaniel, V. Shlyaptseva, T. Adkins, and C. Meyer, "Properties of planar wire arrays Z-pinch source and comparison with cylindrical arrays," High Energy Density Phys. **3**, 136 (2007).
[38]V. V. Ivanov, V. I. Sotnikov, A. Haboub, A. P. Shevelko, A. L. Astanovitskiy, A. Morozov, E. D. Kazakov, and S. Altemara, "Mitigation of plasma implosion inhomogeneity in 'star'-like wire array z-pinches," Phys. Rev. Lett. **100**, 025004 (2008).
[39]S. V. Lebedev, D. J. Ampleford, S. N. Bland, S. C. Bott, J. P. Chittenden, J. Goyer, C. Jennings, M. G. Haines, G. N. Hall, D. A. Hammer, J. B. A. Palmer, S. A. Pikuz, T. A. Shelkovenko, and T. Christoudias, Plasma Phys. Control. Fusion **47**, A91 (2005).
[40]D. B. Sinars *et al.*, Phys. Rev. Lett. **93**, 145002 (2004).
[41]A. Haboub, V. V. Ivanov, A. L. Astanovitskiy, A. A. Morozov, and S. D. Altemara, IEEE Trans. Plasma Sci. **36**(4), 1290 (2008).
[42]V. V. Ivanov, V. I. Sotnikov, A. Haboub, G. E. Sarkisov, R. Presura, and T. E. Cowan, Phys. Plasmas **14**, 032703 (2007).
[43]T. W. L. Sanford, M. E. Cuneo, D. E. Bliss, C. A. Jennings, R. C. Mock, T. J. Nash, W. A. Stygar, and E. M. Waisman, Phys. Plasmas **14**, 052703 (2007).
[44]S. V. Lebedev, R. Aliaga-Rossel, S. N. Bland, J. P. Chittenden, A. E. Dangor, M. G. Haines, and M. Zakaullah, Phys. Rev. Lett. **84**, 1708 (2000).
[45]V. V. Ivanov, A. L. Astanovitskiy, D. Papp, J. P. Chittenden, S. N. Bland, B. Jones, and S. D. Altemara, "Study of transparent and non-transparent regimes of implosion in star wire arrays," Phys. Plasmas **17**, 102702 (2010).
[46]A. L. Velikovich, I. V. Sokolov, and A. A. Esaulov, Phys. Plasmas **9**, 1366 (2002).
[47]J. Davis, N. A. Gondarenko, and A. L. Velikovich, Appl. Phys. Lett. **70**, 170 (1997).
[48]S. V. Lebedev, F. N. Beg, S. N. Bland, J. P. Chittenden, A. E. Dangor, M. G. Haines, K. H. Kwek, S. A. Pikuz, and T. A. Shelkovenko, Phys. Plasmas **8**, 3734 (2001).
[49]M. E. Cuneo, E. M. Waisman, S. V. Lebedev, J. P. Chittenden, W. A. Stygar *et al.*, Phys. Rev. E **71**, 046406 (2005).
[50]B. Jones, C. A. Coverdale, C. Deeney, D. B. Sinars, E. M. Waisman, M. E. Cuneo, D. J. Ampleford, P. D. LePell *et al.*, Phys. Plasmas **15**, 122703 (2008).
[51]D. Papp, V. V. Ivanov, B. Jones, A. Haboub, A. A. Anderson, S. D. Altemara, and B. R. Talbot, Phys. Plasmas **19**, 092704 (2012).
[52]S. V. Lebedev, F. N. Beg, S. N. Bland, J. P. Chittenden, A. E. Dangor, M. G. Haines, S. A. Pikuz, and T. A. Shelkovenko, Laser Part. Beams **19**, 355 (2001).
[53]G. F. Swadling, S. V. Lebedev, G. N. Hall, F. Suzuki-Vidal, G. Burdiak, A. J. Harvey-Thompson, S. N. Bland, P. De Grouchy, E. Khoory *et al.*, Phys. Plasmas **20**, 062706 (2013).
[54]M. Sherlock, J. P. Chittenden, S. V. Lebedev, and M. G. Haines, "Ion collisions and the Z-pinch precursor column," Phys. Plasmas **11**(4), 1609–1616 (2004).
[55]R. H. Lehmberg and J. A. Stamper, "Depolarization in laser probing of inhomogeneous magnetized plasmas," Phys. Fluids **21**(5), 814–816 (1978).
[56]V. V. Ivanov, J. P. Chittenden, S. D. Altemara, N. Niasse, P. Hakel, R. C. Mancini, D. Papp, and A. A. Anderson, "Study of the internal structure and small-scale instabilities in the dense Z pinch," Phys. Rev. Lett. **107**, 165002 (2011).
[57]V. L. Kantsyrev, A. S. Chuvatin, A. A. Esaulov *et al.*, Phys. Plasmas **20**, 070702 (2013).
[58]S. A. Pikuz, D. B. Sinars, T. A. Shelkovenko, K. M. Chandler, D. A. Hammer, G. V. Ivanenkov, W. Stepniewski, and I. Yu. Skobelev, Phys. Rev. Lett. **89**, 035003 (2002).
[59]D. B. Sinars, R. D. McBride, S. A. Pikuz, T. A. Shelkovenko, D. F. Wenger, M. E. Cuneo, E. P. Yu, J. P. Chittenden, E. C. Harding, S. B. Hansen, B. P. Peyton, D. J. Ampleford, and C. A. Jennings, Phys. Rev. Lett. **109**, 155002 (2012).
[60]V. V. Ivanov, D. Papp, A. A. Anderson, B. R. Talbot, A. L. Astanovitskiy, V. Nalajala, O. Dmitriev, J. P. Chittenden, N. Niasse, S. A. Pikuz, and T. A. Shelkovenko, "Study of micro-pinches in wire-array Z pinches," Phys. Plasmas **20**, 112703 (2013).
[61]G. S. Sarkisov, A. S. Shikanov, B. Etlitcher, S. Attelan, and C. Rouile, JETP Lett. **61**, 485 (1995).
[62]A. A. Anderson, V. V. Ivanov, and D. Papp, "Visualization of the magnetic field and current path in Z-pinch and X-pinch plasmas," High Energy Density Phys. **15**, 1 (2015).